Ocean internal waves interpreted as oscillation travelling waves in consideration of ocean dissipation*

Jiang Zhu-Hui(姜祝辉)[a)b)†], Huang Si-Xun(黄思训)[a)], You Xiao-Bao(游小宝)[b)c)], and Xiao Yi-Guo(肖义国)[b)]

[a)] College of Meteorology and Oceangraphy, PLA University of Science and Technology, Nanjing 211101, China
[b)] Beijing Institute of Applied Meteorology, Beijing 100029, China
[c)] Institute of Atmospheric Physics, Chinese Academy of Sciences, Beijing 100029, China

(Received 8 October 2013; revised manuscript received 13 January 2014; published online 15 April 2014)

Most studies of the synthetic aperture radar remote sensing of ocean internal waves are based on the solitary wave solutions of the Korteweg–de Vries (KdV) equation, and the dissipative term in the KdV equation is not taken into account. However, the dissipative term is very important, both in the synthetic aperture radar images and in ocean models. In this paper, the traveling-wave structure to characterize the ocean internal wave phenomenon is modeled, the results of numerical experiments are advanced, and a theoretical hypothesis of the traveling wave to retrieve the ocean internal wave parameters in the synthetic aperture radar images is introduced.

Keywords: synthetic aperture radar, ocean internal waves, oscillation travelling wave, Korteweg–de Vries equation

PACS: 03.65.Ge, 42.79.Qx **DOI:** 10.1088/1674-1056/23/5/050302

1. Introduction

Ocean internal waves play an important role in ocean dynamics.[1] Through *in situ* observations of the Andaman Sea, Osborne *et al.*[2] depicted ocean internal waves with the solitary wave solution of the Korteweg–de Vries (KdV) equation, and put forward the relationship between the ocean internal waves and a surface wave model. Alpers[3] studied the ocean internal wave remote sensing mechanism of synthetic aperture radar images equipped on Seasat. Liu *et al.*[4] studied the ocean internal waves in the east of Taiwan. Based on the solitary wave solution of the KdV equation, Zheng *et al.*[5] theoretically derived the expression of the scattering cross section and the internal wave parameters through the synthetic aperture radar data, and then gave a method for calculating the half-width and amplitude of the internal waves. Ji *et al.*[6] proposed a quick and exact synthetic aperture radar imaging method for one-dimensional layered rough surfaces, and Song[7] advanced a set of Boussinesq-type equations for the interfacial internal waves in a two-layer stratified fluid, which provided a new view on synthetic aperture radar imaging and internal wave stratification. Yang *et al.*[8] introduced a numerical model, which consisted of the KdV equation, the spectrum equilibrium equation, and the Bragg scattering model, to study the relationship between different frequencies and synthetic aperture radar internal wave strengths. Jackson[9] utilized synthetic aperture radar images to determine parameters such as the internal wave phase velocity, and used the retrieved parameters to estimate the high-frequency nonlinear wave location. The above studies are based on the solitary wave solutions of the KdV equation, and do not take the dissipative term in the KdV equation into account. Meanwhile, Liu's study[10] showed that the dissipative term impacts on the ocean internal waves. This paper introduces the existing hydrodynamic theory of synthetic aperture radar images, and the imaging mechanism is analyzed through numerical experiments (Section 2). The theoretical model of a traveling wave to characterize the ocean internal waves is put forward, and the numerical experiment results are brought forward in Section 3. Lastly, for the KdV equation traveling wave solutions, a theoretical hypothesis to retrieve the internal wave parameters using synthetic aperture radar images is suggested in Section 4.

2. Solitary wave imaging theory of ocean internal wave in synthetic aperture radar images

The movement of water particles in ocean internal waves is bigger near the thermocline and is smaller farther away from the thermocline. This movement causes the changes of magnitude and direction of the ocean surface flow, and leads to the divergence and convergence of the surface water particles. The sea surface roughness changes due to the interaction of the surface flow and the surface wave. Eventually, the alternately dark and bright internal wave trains are shown in the synthetic aperture radar images. The theoretical model of the synthetic aperture radar remote sensing internal wave is introduced, and the relationship between the internal wave and the

*Project supported by the High Resolution Earth Observation Major Special Project of Youth Innovation Foundation of China (Grant No. GFZX04060103-3-12) and the National Natural Science Foundation of China (Grant No. 41175025).

†Corresponding author. E-mail: jiangzhuhui@sina.com

© 2014 Chinese Physical Society and IOP Publishing Ltd

synthetic aperture radar backscatter cross section is revealed through numerical experiments.

2.1. Theoretical model

The theoretical model of synthetic aperture radar remote sensing internal wave consists of the KdV equation, the wave number spectral density of the high-frequency ocean surface wave field, and the Bragg scattering model.

The evolution of the internal waves is described by the KdV equation

$$\frac{\partial \eta}{\partial t}+\left(C_0+\alpha\eta+\alpha_1\eta^2\right)\frac{\partial \eta}{\partial x}+\beta\frac{\partial^3\eta}{\partial x^3}+\kappa\eta-\varepsilon\frac{\partial^2\eta}{\partial x^2}=0, \quad (1)$$

where $\eta(t,x)$ is the wave elevation, t is the time, C_0 is the linear wave speed, parameters α, α_1, β, κ, and ε are the coefficients for the nonlinear, higher-order nonlinear, dispersion, shoaling, and dissipation effects, and x is the horizontal displacement.

For a two-layer system with a mixed layer h_1 thick and a bottom layer h_2 thick, the density difference between the two layers is $\Delta\rho=\rho_2-\rho_1$, where ρ is the density of water, and g is the gravity acceleration.

Due to the complexity, equation (1) is generally solved after reasonable simplifications. Liu *et al.*,[4] Zheng *et al.*,[5] Lamb *et al.*,[11] Yang *et al.*,[8] and Li *et al.*[1] assume $\alpha_1=\kappa=\varepsilon=0$, and the KdV equation is simplified to

$$\frac{\partial \eta}{\partial t}+\left(C_0+\alpha\eta\right)\frac{\partial \eta}{\partial x}+\beta\frac{\partial^3\eta}{\partial x^3}=0, \quad (2)$$

so the solitary wave solution is

$$\eta(x,t)=\pm\eta_0\,\mathrm{sech}^2\left(\frac{x-C_\mathrm{p}t}{l}\right), \quad (3)$$

where η_0 is the wave amplitude. When the mixed layer is thinner than the bottom layer, $h_1<h_2$, only the depression waves can be evolved, and $\eta(x,t)<0$. When the mixed layer is thicker than the bottom layer, $h_1>h_2$, only the elevation waves can be evolved, and $\eta(x,t)>0$. The wave speed is given by

$$C_\mathrm{p}=C_0+\frac{\alpha\eta_0}{3}=C_0\left[1+\frac{\eta_0\left(h_2-h_1\right)}{2h_1h_2}\right],$$

the half width is given by

$$l=\frac{2h_1h_2}{\sqrt{3\eta_0\left|h_2-h_1\right|}}.$$

The horizontal velocity of the surface current induced by the solitary internal wave is[5]

$$u_1(x,t)=\pm\frac{C_0\eta_0}{h_1}\,\mathrm{sech}^2\left[\frac{x-C_\mathrm{p}t}{l}\right]. \quad (4)$$

Yuan[12] described the wave number spectral density of the high-frequency ocean surface wave field as

$$\psi(k)=\begin{cases} m_3^{-1}\left[m\left(\dfrac{u_*}{C_\mathrm{p}}\right)^2-4\upsilon k^2\omega^{-1}-S_{\alpha\beta}\dfrac{\partial U_\beta}{\partial x_\alpha}\omega^{-1}\right]k^{-4}, \\ m_4^{-\frac{1}{2}}\left[m\left(\dfrac{u_*}{C_\mathrm{p}}\right)^2-4\upsilon k^2\omega^{-1}-S_{\alpha\beta}\dfrac{\partial U_\beta}{\partial x_\alpha}\omega^{-1}\right]^{\frac{1}{2}}k^{-4}, \end{cases}$$

where the dimensionless constant $m=0.04$, m_3 and m_4 are dimensionless constant coefficients to be determined, υ is the viscosity of the seawater, ω is the angular frequency of the ocean surface waves, k is the wave number of the ocean surface waves, and u_* is the friction velocity. The wind speed obtained from numerical models, buoys, or the spaceborne detector generally refers to the wind speed 10 m above the sea surface. We use the empirical relationship proposed by Amorocho *et al.*[13] to obtain the relation between u_* and U_{10}, when $U_{10}<7$ m/s, $u_*\approx 0.034U_{10}$.

The synthetic aperture radar backscatter cross section can be expressed as

$$\sigma^\mathrm{o}(\theta)_{ij}=16\pi k_\mathrm{o}^4\left|g_{ij}(\theta)\right|^2\psi(0,2k_\mathrm{o}\sin\theta), \quad (5)$$

where θ is the synthetic aperture radar incidence angle, and k_o is the radar wave number. Synthetic aperture radar imaging satisfies the Bragg resonant scatter and, on the condition of horizontal and vertical polarizations,

$$\begin{cases} g_\mathrm{HH}(\theta)=\dfrac{\left(\varepsilon_\mathrm{r}-1\right)\cos^2\theta}{\left[\cos\theta+\left(\varepsilon_\mathrm{r}-\sin^2\theta\right)^{\frac{1}{2}}\right]^2}, \\ g_\mathrm{VV}(\theta)=\dfrac{\left(\varepsilon_\mathrm{r}-1\right)\left[\varepsilon_\mathrm{r}\left(1+\sin^2\theta\right)-\sin^2\theta\right]\cos^2\theta}{\left[\varepsilon_\mathrm{r}\cos\theta+\left(\varepsilon_\mathrm{r}-\sin^2\theta\right)^{\frac{1}{2}}\right]^2}, \end{cases} \quad (6)$$

where ε_r is the relative dielectric constant of the seawater. Zheng *et al.*[5] gives

$$S_{\alpha\beta}\frac{\partial U_\beta}{\partial x_\alpha}=\frac{1}{2}\left[\frac{\partial u}{\partial x}\cos^2\varphi+\left(\frac{\partial u}{\partial y}+\frac{\partial v}{\partial x}\right)\cos\varphi\sin\varphi+\frac{\partial v}{\partial x}\sin^2\varphi\right], \quad (7)$$

where u and v are the velocity components, and φ is the wave direction. From Eqs. (3)–(7), Li *et al.*[14] derive the formula for the C-band synthetic aperture radar remote sensing ocean internal wave

$$\Delta\sigma^\mathrm{o}\,[\mathrm{dB}]=10\lg\left[1-\frac{C_0\eta}{h_1l\omega}\mathrm{th}\left(\frac{x-C_\mathrm{p}t}{l}\right)\frac{\cos^2\varphi}{\left[m\left(\dfrac{u_*}{c}\right)^2\right]}\right]. \quad (8)$$

2.2. Ocean internal solitary wave and its simulation on the synthetic aperture radar image

A simulation is carried out to test this theoretical model. Figure 1 shows the elevation solitary wave and its synthetic aperture radar image intensity variation. Figure 2 shows the depression solitary wave and its synthetic aperture radar image intensity variation. Let $X = x - C_p t$, $\varphi = 23^\circ$, $\theta = 23^\circ$, $g = 9.8$ m/s^2, $\rho = 1025$ kg/m^3, $\Delta\rho = 3$ kg/m^3, $\eta_0 = 8$ m, $h_1 = 20$ m, $h_2 = 30$ m, $U_{10} = 2$ m/s, and assume the synthetic aperture radar work on the C band and the radar wave number $k_o = 17.5439$ m^{-1}.

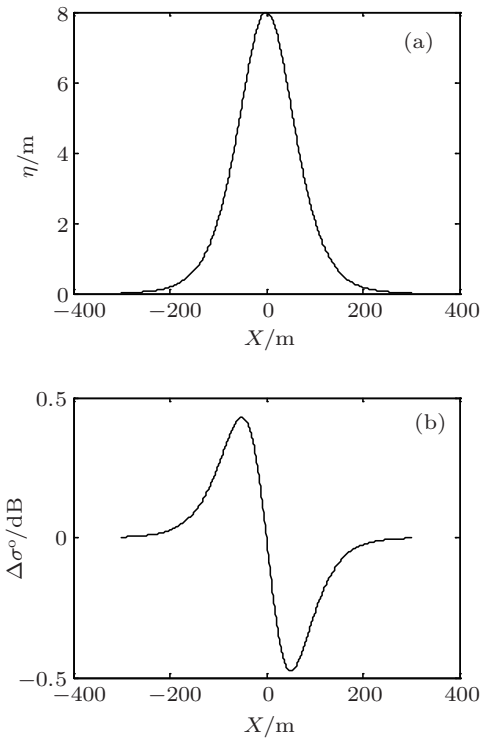


Fig. 1. (a) Elevation solitary wave and (b) synthetic aperture radar image intensity variation.

Figure 1(a) shows a typical elevation solitary wave, and Figure 1(b) shows the corresponding synthetic aperture radar image intensity variation. The $\Delta\sigma^o$ gradually increases to a maximum, it then decreases to a very small value, and finally comes close to zero. When the solitary wave comes to the maximum, the corresponding $\Delta\sigma^o$ is close to 0 dB, when the solitary wave is ascending, $\Delta\sigma^o$ comes to the maximum, and when the solitary wave is descending, $\Delta\sigma^o$ comes to the minimum. This is because the ascending solitary wave causes a convergent surface flow, and $\Delta\sigma^o$ achieves the maximum, thus a light wave packet presents in the synthetic aperture radar images. The descending solitary wave causes a divergent surface flow, and $\Delta\sigma^o$ achieves the minimum, thus a dark wave packet presents in the synthetic aperture radar images. Figure 2(a) shows a typical depression solitary wave, and Figure 2(b) shows the corresponding synthetic aperture radar image intensity variation. Apparently, Figure 2 is the reverse of Figure 1, $\Delta\sigma^o$ gradually decreases to a minimum, and then comes to the maximum. The imaging mechanism is the same, the convergency of the solitary wave leads to the bright packet on the synthetic aperture radar image, and the divergency of the solitary wave leads to the dark packet on the synthetic aperture radar image.

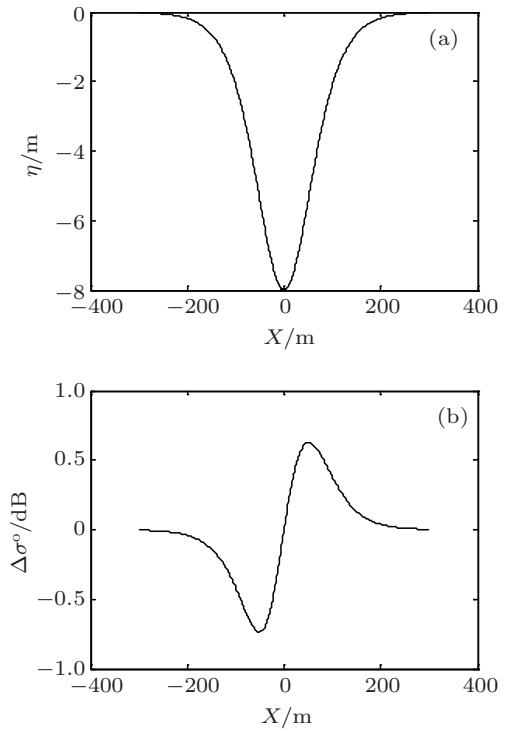


Fig. 2. (a) Depression solitary wave and (b) synthetic aperture radar image intensity variation.

3. The traveling wave theory of the ocean internal wave

The research above is based on the dissipation coefficient in the KdV equation approaching to 0. However, ocean dissipation exists, and it is not always a small quantity. The simplified KdV equation (2) only considers the interaction between nonlinearity and dispersion, while it ignores the dissipative effect. Thus, the solitary wave solutions of the KdV equation cannot fully reflect the ocean internal wave characteristics.

Liu *et al.*[4] advanced a schematic diagram showing nonlinear surface expressions where the wave amplitude increases gradually along the propagation direction; however, the solitary internal wave cannot explain this phenomenon. In order to research the internal wave propagation mechanism and the internal wave trains in the synthetic aperture radar image, we add ε into Formula (2) on the condition of $h_1 < h_2$,

$$\frac{\partial \eta}{\partial t} + (C_0 + \alpha\eta)\frac{\partial \eta}{\partial x} + \beta\frac{\partial^3 \eta}{\partial x^3} - \varepsilon\frac{\partial^2 \eta}{\partial x^2} = 0, \tag{9}$$

for $h_1 > h_2$, the result is similar.

3.1. The analytical model

We discuss the travelling wave of Formula (9) below. Assume

$$\eta = U(\theta) + h_2, \quad \theta = C_{\mathrm{p}} t - x, \quad U' = \mathrm{d}U/\mathrm{d}\theta. \tag{10}$$

Substituting formula (10) into Eq. (9) yields

$$\left[C_{\mathrm{p}} - C_0 - \alpha\left(U + h_2\right)\right] U' - \beta U''' - \varepsilon U'' = 0.$$

Suppose the property of $\theta \to +\infty$, we have $U = U' = U'' = 0$ in the infinite point. Integrating the above formulas leads to

$$\begin{aligned} &\left(C_{\mathrm{p}} - C_0\right)\left(U + h_2\right) - \frac{\alpha}{2}\left(U + h_2\right)^2 - \beta U'' - \varepsilon U' \\ =\ &\left(C_{\mathrm{p}} - C_0\right) h_2 - \frac{\alpha}{2} h_2^2, \end{aligned}$$

hence

$$\left[\left(C_{\mathrm{p}} - C_0 - \alpha h_2\right) U - \frac{\alpha}{2} U^2\right] - \beta U'' - \varepsilon U' = 0. \tag{11}$$

Asumme

$$\begin{cases} A = C_{\mathrm{p}} - C_0 - \alpha h_2, \\ \mu = \dfrac{\varepsilon}{\beta}, \\ f(U) = \dfrac{1}{\beta}\left(AU - \frac{\alpha}{2} U^2\right) = -\dfrac{\alpha}{2\beta} U\left(U - U_1\right), \\ U_1 = \dfrac{2}{\alpha} A. \end{cases} \tag{12}$$

Substituting Formula (12) into Eq. (11) yields

$$\begin{cases} U'' + \mu U' = \dfrac{1}{\beta}\left(AU - \dfrac{\alpha}{2} U^2\right) = f(U), \\ U\,|_{\theta=0} = 0, \\ U'\,|_{\theta=0} = 0. \end{cases} \tag{13}$$

For convenience, we assume $A = C_{\mathrm{p}} - C_0 - \alpha h_2 > 0$, so $\alpha < 0$, and

$$U_1 = \frac{2}{\alpha} A < 0. \tag{14}$$

Then, equation (13) becomes an equivalent nonlinear ODES

$$\begin{cases} U' = P, \\ P' = -\mu P + f(U). \end{cases} \tag{15}$$

And, from Eq. (16), we have

$$\frac{\mathrm{d}P}{\mathrm{d}U} = -\mu + \frac{f(U)}{P}, \quad P\,|_{U=0} = 0.$$

Section 4 will use the initial value

$$\frac{\mathrm{d}P}{\mathrm{d}U}\,|_{U=0} = \frac{1}{2}\left(-\mu + \sqrt{\mu^2 + \frac{4A}{\beta}}\right)$$

to carry out further numerical experiments.

The equilibrium points of Eq. (16) have $P = 0$ and $f(U) = -\frac{\alpha}{2\beta} U\left(U - U_1\right) = 0$, so there are two equilibrium points $(0,0)$ and $(U_1, 0)$. Now we will deal with the properties of the equilibrium points.

The linearized ODES of Eq. (16) near equilibrium point $(0,0)$ are

$$\begin{cases} \begin{pmatrix} U \\ P \end{pmatrix}' = \begin{pmatrix} 0 & 1 \\ f'(0) & -\mu \end{pmatrix} \begin{pmatrix} U \\ P \end{pmatrix}, \\ f'(0) = \dfrac{A}{\beta} > 0. \end{cases} \tag{16}$$

And the characteristic equation is $\lambda^2 + \lambda\mu - A/\beta = 0$, with the characteristic roots being

$$\lambda_{1,2} = \frac{1}{2}\left(-\mu \pm \sqrt{\mu^2 + \frac{4A}{\beta}}\right).$$

Since $A > 0$, the characteristic roots are real with different signs; therefore, point $(0,0)$ is the saddle point (see Fig. 3), and is also the saddle point of the nonlinear ODES (14).

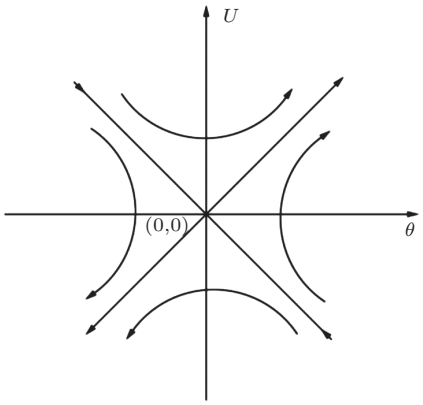


Fig. 3. Schematic diagram of equilibrium point $(0,0)$.

The linearized ODES of Eq. (16) near equilibrium point $(U_1, 0)$ are

$$\begin{cases} \begin{pmatrix} U \\ P \end{pmatrix}' = \begin{pmatrix} 0 & 1 \\ f'(U_1) & -\mu \end{pmatrix} \begin{pmatrix} U - U_1 \\ P \end{pmatrix}, \\ f'(U_1) = \frac{1}{\beta}(A - \alpha U)\,|_{U_1} > 0. \end{cases} \tag{17}$$

The characteristic equation is

$$\begin{vmatrix} \lambda & -1 \\ \dfrac{A}{\beta} & \lambda + \mu \end{vmatrix} = \lambda^2 + \mu\lambda + \frac{A}{\beta} = 0,$$

with the characteristic roots being

$$\lambda_{1,2} = \frac{1}{2}\left(-\mu \pm \sqrt{\mu^2 - \frac{4A}{\beta}}\right).$$

When there is no dissipation, $\mu = 0$ corresponds to $\lambda = \pm \mathrm{i}\sqrt{A/\beta}$, $(U_1, 0)$ is the center of Eq. (17) (see Fig. 4). When

there is small dissipation $\mu^2 \geq 4A/\beta$, $(U_1,0)$ is the stable focus of Eq. (17), and is also that of Eq. (16) (see Fig. 5). When there is large dissipation $\mu^2 \geq 4A/\beta$, $(U_1,0)$ is the stable node of Eq. (17) and of Eq. (16) (see Fig. 6).

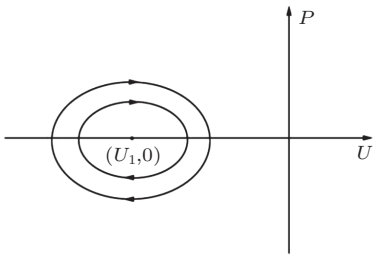


Fig. 4. Schematic diagram of equilibrium point $(U_1,0)$ in the case of $\mu = 0$.

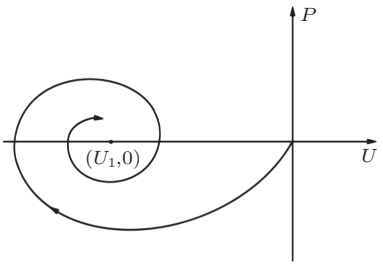


Fig. 5. Schematic diagram of equilibrium point $(U_1,0)$ in the case of $\mu^2 < 4A/\beta$.

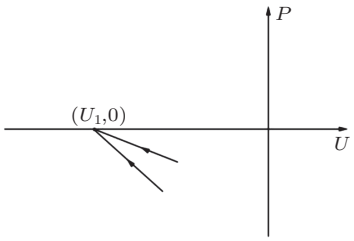


Fig. 6. Schematic diagram of equilibrium point $(U_1,0)$ in the case of $\mu^2 \geq 4A/\beta$.

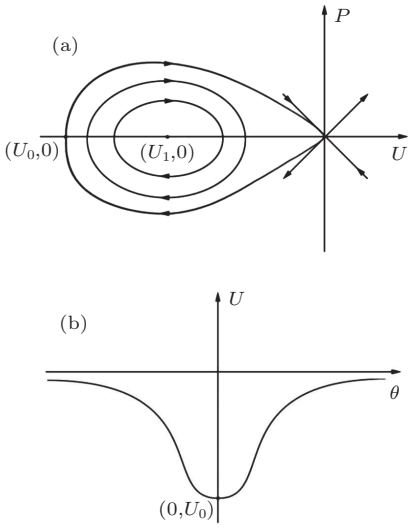


Fig. 7. Schematic diagram of trajectory in the case of $\mu = 0$: (a) on plane (U,P), (b) on plane (θ,U).

Considering the three cases above, there are three solutions of Eq. (16).

Case 1 There is no dissipation $\mu = 0$. Figure 7(a) is a schematic diagram of the trajectory of the phase plane (U,P) in the case of $\mu = 0$, $(U_1,0)$ is the center. If $P(U)$ starts from (0,0), the trajectory will return to (0,0), realizing the self-connection of the saddle point, which is a homoclinic orbit. For the homoclinic orbit, $(U_0,0)$ is the minimum point of U. In the beginning, if θ increases, then U decreases, until $\theta = 0$, $U = U_0$ is the minimum point, then U gradually increases (Fig. 7(b)). In this case, the solution of Eq. (16) is in the form of a solitary wave.

Case 2 There is small dissipation$\mu^2 < 4A/\beta$. Figure 8(a) is a schematic diagram of the trajectory of the phase plane (U,P) in the case of $\mu^2 < 4A/\beta$, $(U_1,0)$ is a stable focus. If $P(U)$ starts from (0,0), the trajectory will twist to stable focus $(U_1,0)$, realizing the connection of the saddle point and the focus point. In the beginning, if θ increases, then U decreases, until $\theta = 0$, U comes to its minimum point, then U oscillates during travelling, and the amplitude gradually diminishes (Fig. 8(b)). In this case, the solution of Eq. (16) is in the form of an oscillation travelling wave.

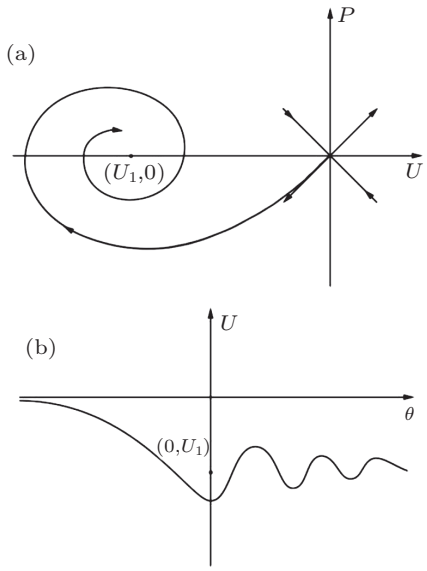


Fig. 8. Schematic diagram of trajectory in the case of $\mu^2 < 4A/\beta$: (a) on plane (U,P), (b) on plane (θ,U).

Case 3 There is large dissipation $\mu^2 \geq 4A/\beta$. Figure 9(a) is a schematic diagram of the trajectory of the phase plane (U,P) in the case of $\mu^2 \geq 4A/\beta$, $(U_1,0)$ is a stable node. If $P(U)$ starts from (0,0), then the trajectory will go to the stable node $(U_1,0)$, realizing the connection of the saddle point and the node point. In the beginning, if θ increases, then U decreases, until $\theta \to -\infty$, U comes to its minimum point U_1 (Fig. 8(b)). In this case, the solution of Eq. (16) is in the form of a monotone travelling wave.

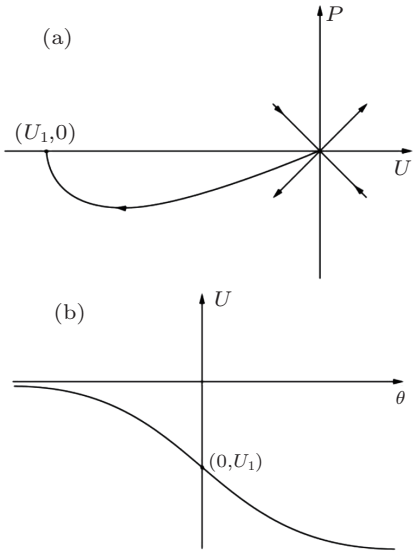


Fig. 9. Schematic diagram of trajectory in the case of $\mu^2 \geq 4A/\beta$: (a) on plane (U,P), (b) on plane (θ,U).

3.2. Analysis of the homoclinic orbit

For $\mu = 0$, i.e., $\varepsilon = 0$, $(0,0)$ is the saddle point, and $(U_1,0)$ is the center, the nonlinear ODES (16) is retrograded into

$$U'' = f(U) = \frac{1}{\beta}\left(AU - \frac{\alpha}{2}U^2\right), \tag{18}$$

$$U''U' = \frac{1}{\beta}\left(AU - \frac{\alpha}{2}U^2\right)U'.$$

Owing to $\lim\limits_{\theta\to\infty} U = 0$ and $\lim\limits_{\theta\to\infty} U' = 0$, integrating Eq. (18) yields (Fig. 10)

$$U'^2 = \frac{2}{\beta}\left(\frac{A}{2}U^2 - \frac{\alpha}{6}U^3\right) = -\frac{\alpha}{3\beta}U^2\left(U - \frac{3A}{\alpha}\right) = G(U). \tag{19}$$

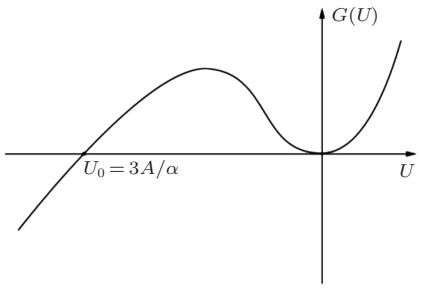


Fig. 10. Schematic diagram of $G(U)$.

Let $U_0 = 3A/\alpha < 0$, from (U_0,θ_0), if θ increases, U increases. We have

$$\int_{U_0}^{U} \frac{\mathrm{d}U}{-U\sqrt{U-U_0}} = \sqrt{\frac{-\alpha}{3\beta}}\theta. \tag{20}$$

Assume $U - U_0 = t^2$, $\mathrm{d}U = 2t\,\mathrm{d}t$, then

$$\int_{U_0}^{U} \frac{\mathrm{d}U}{-U\sqrt{U-U_0}} = -\int_0^{\sqrt{U-U_0}} \frac{2\,\mathrm{d}t}{(t^2 - U_0)}$$

$$-2\int_0^{\sqrt{U-U_0}} \frac{\mathrm{d}t}{\left(t^2 - \sqrt{U_0}^2\right)}$$

$$= 2\frac{1}{2\sqrt{-U_0}^2}\ln\left|\frac{t+\sqrt{-U_0}}{t-\sqrt{-U_0}}\right|\Bigg|_0^{\sqrt{U-U_0}}$$

$$= \frac{1}{\sqrt{-U_0}}\ln\left|\frac{\sqrt{U-U_0}+\sqrt{-U_0}}{-\sqrt{U-U_0}+\sqrt{-U_0}}\right| = \sqrt{-\frac{\alpha}{3\beta}}\theta. \tag{21}$$

Let $X = \sqrt{\alpha U_0/3\beta}$, then we can obtain

$$\sqrt{U-U_0}+\sqrt{-U_0} = \mathrm{e}^X\left(-\sqrt{U-U_0}+\sqrt{-U_0}\right),$$

so

$$U - U_0 = \left(\frac{\mathrm{e}^{\frac{X}{2}} - \mathrm{e}^{-\frac{X}{2}}}{\mathrm{e}^{\frac{X}{2}} + \mathrm{e}^{-\frac{X}{2}}}\right)^2(-U_0) = \left(\mathrm{th}^2\frac{X}{2}\right)(-U_0).$$

Thus

$$U = U_0\left(1 - \mathrm{th}^2\frac{X}{2}\right) = U_0\,\mathrm{sech}^2\frac{X}{2} = U_0\,\mathrm{sech}^2\frac{ct-x}{\Delta},$$

where

$$\Delta = \sqrt{\frac{12\beta}{\alpha U_0}}. \tag{22}$$

If U_0 is known, the solitary wave speed is $A = \frac{\alpha}{3}U_0 = C_\mathrm{p} - C_0 - \alpha h_2$, and

$$C_\mathrm{p} = C_0 + \alpha\left(\frac{U_0}{3} + h_2\right). \tag{23}$$

Equation (23) is different from $C_\mathrm{p} = C_0 + \alpha U_0/3$, which is the result of Zheng *et al.*[5] and Liu.[10]

3.3. Analysis of the saddle focus

In this section, we will prove that for $0 < \mu^2 < 4A/\beta$, there exists a unique oscillation travelling wave with $(0,0)$ being the saddle point and $(U_1,0)$ being the stable focus. We use the idea from Refs. [15]– [17].

Theorem 1 For $0 < \mu^2 < 4A/\beta$, there exists an oscillation travelling wave and $\lim\limits_{\theta\to-\infty} U(\theta) = 0$, $\lim\limits_{\theta\to+\infty} U(\theta) = U_1$.

As mentioned above, for $\mu = 0$, there exists a homoclinic orbit $P_0(U)$. First, if $\mu_1 < \mu_2$, $P_1(U) < P_2(U)$ near the point of $(0,0)$ in the third quadrant, where $U \in (-\delta,0)$, $P_1(0) = P_2(0)$, and δ is a sufficiently small positive number. Because

$$\frac{\mathrm{d}P_i(U)}{\mathrm{d}U} = -\mu_i + \frac{f(U)}{P_i}, \quad (i = 1,2), \tag{24}$$

then

$$\frac{\mathrm{d}(P_1 - P_2)}{\mathrm{d}U} + \frac{f(U)}{P_1P_2}(P_1 - P_2) = -(\mu_1 - \mu_2),$$

thus

$$\frac{\mathrm{d}}{\mathrm{d}U}\left[\int \mathrm{e}^{(P_1-P_2)}\right] = -(\mu_1 - \mu_2)\exp\left(\int_{-\delta}^{U}\frac{f(\tau)}{P_1P_2}\mathrm{d}\tau\right).$$

Let

$$W(U) = \exp\left(\int_{-\delta}^{U} \frac{f(\tau)}{P_1 P_2}\,\mathrm{d}\tau\right),$$

$$(P_1 - P_2)\,W(U) = Z(U),$$

then

$$\frac{\mathrm{d}Z(U)}{\mathrm{d}U} = (\mu_2 - \mu_1)\,W(U). \tag{25}$$

Since $f(\tau) < 0$ and $P_i(\tau) < 0$ for $\tau \in (-\delta, 0)$ and $P_1(\tau)P_2(\tau)$ has a second-order zero point at $\tau = 0$, $\lim\limits_{U\to 0} W(U) = 0$, that is, $W(0) = 0$. From Eq. (25), we know $Z(U) < 0$, ($U \in (-\delta, 0)$, i.e., $P_1(U) < P_2(U), (U \in (-\delta, 0))$), then $P_\mu(U)$ is monotonously increasing within $U \in (-\delta, 0)$ with respect to μ. Thus, for $U \in (-\delta, 0)$, the trajectory of $\mu \in (\mu_1, \mu_2)$ has

$$P_0(U) < P_{\mu_1}(U) < P_\mu(U) < P_{\mu_2}(U).$$

Therefore, the trajectory of $P_\mu(U)$ intersects with the AB segment (Fig. 11), and is contained in $P_0(U)$.

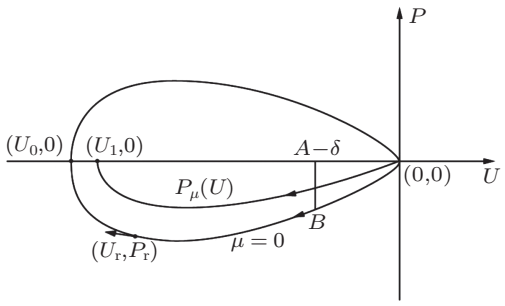


Fig. 11. The $P(U)$ in the phase plane.

Second, the trajectory of $P_\mu(U)$ cannot intersect with, or be tangent to, $P_0(U)$ within the third quadrant. If the trajectory intersected with, or was tangent to, $P_0(U)$ at (U_r, P_r) (Fig. 11), then

$$\frac{\mathrm{d}P_\mu(U)}{\mathrm{d}U}\Big|_{(U_r,P_r)} = -\mu + \frac{f(U_r)}{P(U_r)} < \frac{f(U_r)}{P(U_r)} = \frac{\mathrm{d}P_U(U)}{\mathrm{d}U}\Big|_{(U_r,P_r)},$$

which cannot hold, so $P_\mu(U)$ cannot intersect with, or be tangent to, $P_0(U)$ within the third quadrant.

Third, the trajectory of $P_\mu(U)$ cannot intersect with the P axis for $U \in (U_1, -\delta)$, we draw a line L from $(U_1, 0)$, such that $P = -\gamma(U - U_1)$, $(0 < \gamma \le 1)$, $U \in (U_1, -\delta)$, in which γ is a sufficiently small number. Line L intersects with AB ($U = -\delta$) at C. We put Δ as the zone surrounded by L and $P = 0$, $x = -\delta$, then within $P = 0$ and $x = -\delta$, we have

$$\begin{aligned}\frac{\mathrm{d}P}{\mathrm{d}U} &= -\mu + \frac{-f(U)}{-P(U)} \ge -\mu + \frac{-f(U)}{\gamma(U - U_1)} \\ &= -\mu + \frac{\frac{\alpha}{2\beta}U(U - U_1)}{\gamma(U - U_1)} = -\mu + \frac{\alpha U}{2\beta\gamma}.\end{aligned}$$

Since $U < -\delta$ and $\alpha U > -\alpha\delta$, hence

$$\frac{\mathrm{d}P}{\mathrm{d}U} \ge -\mu - \frac{\alpha\delta}{2\beta\gamma}.$$

The γ should follows $\mathrm{d}P/\mathrm{d}U > 0$, that is, $-\mu - \alpha\delta/2\beta\gamma > 0$, or for $0 < \gamma < -\alpha\delta/2\beta\mu$, $\mathrm{d}P/\mathrm{d}U|_\Delta > 0$, that is, the trajectory cannot intersect with $P = 0$.

For $P > 0$, after the trajectory intersects with $U = 0$, $U' > 0$, and the trajectory is within the second quadrant. By using the same method, we can prove that $P_\mu(U)$ cannot intersect with the U axis (see Fig. 12). Therefore, for $\theta \to +\infty$, $P_\mu(U)$ moves to the point of $(U_1, 0)$, thus the oscillation travelling wave solution exists, and its wave pattern is shown in Fig. 8. We can also prove that for $\mu^2 \ge 4A/\beta$, there exists a unique monotone travelling wave. Since ε is a small number in the ocean, the monotone travelling wave will not generally appear, so we do not prove it in this paper.

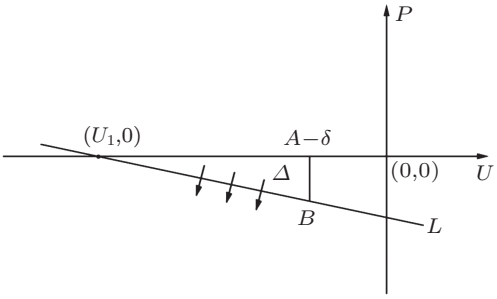


Fig. 12. Schematic diagram of $P(U)$.

3.4. Numerical experiments

Next, we will carry out a numerical experiment to justify the oscillation travelling wave. Liu[10] pointed out that

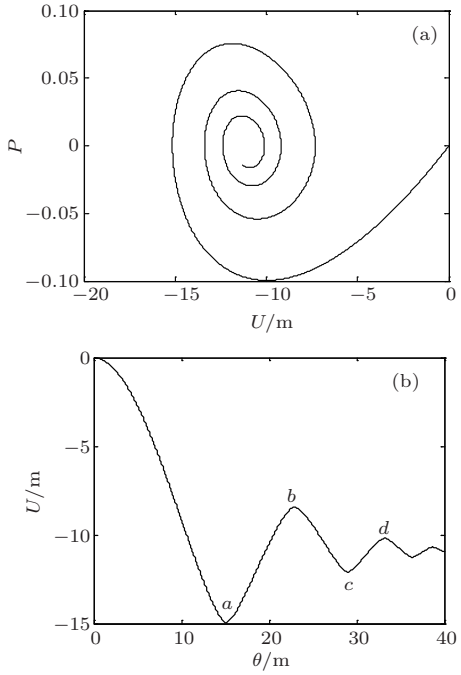


Fig. 13. Numerical experiment for $\varepsilon = 1.0$ m^2/s: (a) P–U, (b) U–θ.

the dissipation coefficient in Sulu sea is about 10 m^2/s, and about 1.0 m^2/s in New York bight, here we assume ε=1.0 m^2/s. Let $h_1 = 30$ m, $h_2 = 110$ m, $C_0 = 0.5$ m/s, $\alpha = -0.018$ s^{-1}, $\beta = 275$ m^3/s, $C_p = -1.38$ m/s, we have $A = C_p - C_0 - \alpha h_2 = 0.10$ m/s from Eq. (12), and $|U_1| = \left|\frac{2}{\alpha}A\right| = 11.1$ m, $\mu = \frac{\varepsilon}{\beta} = 0.00364$ m^{-1}. We can calculate the oscillation travelling wave solution from Eq. (16), see Fig. 13.

Figure 13(a) resembles the schematic diagram of Fig. 8, the minimum point of U is -15 m, and its focus is -11.1 m. If θ increases, the U oscillation travels with the amplitude decrease, this phenomenon matches the case of wave trains in the synthetic aperture radar image.

4. Synthetic aperture radar images of remote sensing ocean internal wave parameters

Li *et al.*,[1] Yang,[8] and Jackson[9] advanced the method of derivation internal wave amplitude, half width, and the depth of stratification from synthetic aperture radar images. However, it is very difficult to retrieve the parameters from the oscillation travelling wave solution, which is more complex than the solution of solitary wave. We can regard the oscillation travelling wave in Fig. 13(b) as a multi-solitary wave, that is, regard *ab* in Fig. 13(b) as an ascending part of the elevation solitary wave, *bc* as a descending part of the depression solitary wave, and *cd* as another ascending part of the elevation solitary wave, and analogically retrieve parameters of every solitary wave. Because of the limited data, we have not utilized real data to retrieve the internal wave parameters, only a concept is advanced, and we look forward to having a positive effect on the internal wave parameter's retrieval.

5. Conclusion

The solitary wave solutions of the KdV equation without a dissipative term cannot explain the phenomenon of wave trains in the synthetic aperture radar images, which are caused by the convergence of the sea surface roughness. We put forward a concept in which the dissipation coefficient is taken into account when we solve the KdV equation. The numerical experiment shows that the solution of an oscillation travelling wave can explain the internal wave trains in the synthetic aperture radar images; thus, the dissipation coefficient should not be ignored. Moreover, a new concept is advanced to retrieve the internal wave parameters from the synthetic aperture radar images.

References

[1] Li H Y, He Y J, Du T and Feng Q Z 2007 *Chinese Marine Environmental Science* **26** 583 (in Chinese)
[2] Osborne A R and Burch T L 1980 *Science* **208** 451
[3] Alpers W 1985 *Nature* **314** 245
[4] Liu A K, Chang Y S, Hsu M K and Liang N K 1998 *J. Geophys. Res.* **103** 7995
[5] Zheng Q, Yuan Y, Klenias V and Yan X H 2001 *J. Geophys. Res.* **106** 31415
[6] Ji W J and Tong C M 2013 *Chin. Phys. B* **22** 020301
[7] Song J B 2006 *Chin. Phys.* **15** 2796
[8] Yang J S, Xiao Q M, Huang W G, Fu B, Chen P and Yao L 2005 *IEEE Trans. Geosci. Remote Sens.* **4** 2588
[9] Jackson C R 2009 *J. Atmos. Ocean. Tech.* **26** 2243
[10] Liu A K 1988 *J. Geophys. Res.* **93** 12317
[11] Lamb K G and Yan L 1996 *Journal of Physical Oceanography* **26** 2712
[12] Yuan Y 1997 *Chin. J. Oceanol. Limnol.* **28** Suppl. 1 (in Chinese)
[13] Amorocho J and DeVries J J 1980 *J. Geophys. Res.* **85** 433
[14] Li H Y, He Y J, Du T and Shen H 2006 *IEEE International Conference on Geoscience and Remote Sensing Symposium* **1** 1319
[15] Huang S X and Zhang M 1993 *Advance in Atmospheric Sciences* **10** 435
[16] Sheng Z and Fang H 2013 *Chin. Phys. B* **22** 029301
[17] Sheng Z 2013 *Chin. Phys. B* **22** 029302